



Crystal structure dependent photocatalytic degradation of manganese and titanium oxides composites

Moushumi Dutta Purkayastha¹ · Shanku Denrah² · Nisha Singh³ · Mitali Sarkar² · Gopala Krishna Darbha^{3,4} · Tapas Pal Majumder¹

Received: 31 December 2019 / Accepted: 19 May 2020 / Published online: 26 May 2020
© Springer Nature Switzerland AG 2020

Abstract

Crystalline hexagonal disk-shaped anatase TiO₂ within manganese oxide (Mn₂O₃) nanorods has been fabricated to form manganese oxide-titanium dioxide (MnT) composites following sonochemical approach. The unique morphology of the synthesized MnT provides higher surface area to enhance the adsorption efficiency and promotes electron-hole separation. This appears particularly promising for efficient photocatalysis. The photocatalytic decolorization efficiency (PD) of sonosynthesized MnT (S-MnT) was tested via decomposition of an organic pollutant, malachite green oxalate under ultraviolet irradiation and compared to that of sol-gel synthesized MnT (H-MnT). The profound impact of hydrogen peroxide (H₂O₂) addition on the photoactivity was tested. S-MnT with addition of sonicated H₂O₂ showed the best photoactivity (PD 99.61% in 50 min) in comparison to sol-gel synthesized H-MnT (PD 92.14% in 60 min). The mechanism of degradation was found to depend on the formation of superoxide radicals (O₂⁻), hydroxyl radicals (·OH) and the defect concentration. The role of ultrasound in the overall degradation process was also discussed. Photoluminescence studies demonstrate that Mn²⁺ ions are in an octahedral and tetrahedral coordination in both the composites which is favourable for light emission.

Keywords Sonosynthesis · Morphology · Hydrogen peroxide · Photocatalysis · Luminescence

1 Introduction

Non-silica mesoporous materials have inspired remarkable research interest as they are expected to serve as novel photocatalysts, semiconductors, electrode materials etc. [1]. Among these novel materials, titanium dioxide (TiO₂) is one among the most investigated functional materials in recent years [2, 3]. Nevertheless, the main problem with TiO₂ photocatalysis lies in the separation of photoinduced

electron-hole pairs. To overcome this issue, different routes have been proposed which include combining the photocatalyst with another transition metal semiconductor [4], incorporation of non-metal ions [5] and by adding some sacrificial agent into the reaction system [6, 7]. Available methods for the formation of the binary composites include the sol-gel route [8], co-precipitation method [9], self-assembly [10] and a chelating agent-assisted precipitation method [11], although each suffers from conventional drawbacks.

Electronic supplementary material The online version of this article (<https://doi.org/10.1007/s42452-020-2933-7>) contains supplementary material, which is available to authorized users.

✉ Tapas Pal Majumder, tpmajumder1966@gmail.com | ¹Department of Physics, University of Kalyani, Kalyani, West Bengal 741235, India. ²Department of Chemistry, University of Kalyani, Kalyani, West Bengal 741235, India. ³Department of Earth Sciences Centre for Climate and Environmental Sciences, Indian Institute of Science, Education and Research Kolkata, Mohanpur, West Bengal 741246, India. ⁴Centre for Climate and Environmental Sciences, Indian Institute of Science, Education and Research Kolkata, Mohanpur, West Bengal 741246, India.



SN Applied Sciences (2020) 2:1126 | <https://doi.org/10.1007/s42452-020-2933-7>

The widely used sol–gel route is characterized by poor dispersion and requirement of complexing agents to control the homogeneous crystallization of dopant inorganic precursors [12] while interfacial self-assembly methods [10] have various technical issues that remain unaddressed. In recent times, sonochemical synthesis of nanocomposites has gained momentum because of its cost-effectiveness and simplicity [13, 14]. Pressure and temperature changes during sonosynthesis result in the production of free radicals that in turn can reduce metal ions to metal or metal oxide nanoparticles [15, 16].

Aquatic ecosystems are continuously being contaminated by dye pollutants and have reached at an alarming point. These organic pollutants can be degraded to benign by-products by advanced oxidation processes which exploit the high reactivity of the hydroxyl radicals (OH^\cdot) as their driving force. The rate of generation of OH^\cdot radical is, however, dependent on the type of crystal polymorphs. It is believed that a correlation exists between the rates of OH^\cdot radical generation and the photocatalytic reactivity [17]. The photoinduced electrons and holes in the photocatalytic process react with H_2O and O_2 to give rise to several reactive oxygen species. Among the various reactive oxygen species, H_2O_2 is the most stable one. It is environment friendly and has high oxidative power [18, 19]. However, its behaviour on semi-conducting particles is very complex. During photocatalytic reactions, it is not only formed but also gets decomposed. Kim et al. [20] have suggested that the difference in the reactivity of anatase and rutile TiO_2 can be ascribed to their adsorption capability of the OH^\cdot radicals. Many researchers have investigated the formation rate of OH^\cdot radicals for various kinds of TiO_2 powders along with the effect of small amounts of H_2O_2 addition [21–24] but none have discussed the method of addition of these agents.

In the present communication, two different $\text{Mn}_2\text{O}_3\text{--TiO}_2$ (MnT) nanocomposites have been synthesized following conventional sol–gel route and an ultrasound assisted cost-effective technique. Two different morphologies, hexagonal nanodisks and nanorods were distinctly observed in the sonosynthesized composite in comparison to sol–gel synthesized composite which showed only hexagonal nanodisks. The focus of this work is to investigate the synergistic photocatalytic degradation of malachite green (MG) in aqueous conditions with addition of H_2O_2 under ultraviolet (UV) irradiation by the synthesized nanocomposites.

2 Experimental section

2.1 Materials required

Titanium (IV) n-butoxide, manganese acetate tetrahydrate was procured from Sigma Aldrich and sodium

hydroxide (NaOH), ethanol, stearic acid, hydrogen peroxide (30% purified) from Merck and malachite green oxalate from PubChem.

2.2 Method of preparation

Ultrasonic irradiation (40 kHz, 480 W) served the base for synthesis of S-MnT nanocomposite. Titanium tetra butoxide (1.0×10^{-2} M) was added drop wise into 100 mL NaOH (1.0×10^{-3} M) in an ice bath. The mixture was then subjected to ultrasonic irradiation using a bath sonicator for a period of 3 h at a temperature of 80 °C. Fresh flow of water was introduced in the bath whenever required to maintain temperature. To this solution, 10 mL ethanolic solution of manganese acetate tetrahydrate (1.0×10^{-1} M) mixed with 0.5 M of melted (80 °C) stearic acid was added and the mixture was subjected to ultrasonic irradiation for 5 h. The final product (S-MnT) was washed with ethanol, filtered and dried at 120 °C for 24 h.

To properly understand the crucial influence of ultrasound governing the nanocomposite synthesis procedure, another MnT was prepared following the sol–gel route. Typically, titanium tetra butoxide (1.0×10^{-2} M) was added drop wise to 100 mL of (1.0×10^{-3} M) NaOH solution and stirred vigorously (700 rev/s) for a period of 4 h. Subsequently, 10 mL of ethanolic solution of manganese acetate tetrahydrate (1.0×10^{-1} M) mixed with 0.5 M of melted (80 °C) stearic acid was added. The contents were put in an autoclave, and heated at 130 °C for 24 h. The obtained product (H-MnT) was filtered, washed thrice with de-ionized water and dried at 200 °C for 5 h.

2.3 Characterization techniques

An X'Pert PRO PANalytical X-ray diffractometer was used to obtain the diffraction patterns of the synthesized materials. Elemental composition and morphology were ascertained with a Field emission Scanning Electron Micrograph (Carl Zeiss SUPRA 55VP Field emission SEM) coupled with an Energy dispersive spectrometer (EDS). Functional groups present in the materials were confirmed with an Infrared (IR) spectrometer (Perkin Elmer Spectrum one L120-000A). The emission and absorption spectra were recorded with a PTI QM 40 spectrometer and UV 3600 spectrometer respectively. A surface area analyser (Micromeritics Gemini VII-2390t) was used to measure the surface area. The samples were degassed at 100 °C and the total pore size distribution (PSD) was measured from the nitrogen desorption isotherm using the cylindrical pore model.

2.4 Degradation experiments

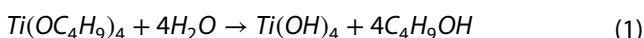
A UV–vis–NIR spectrophotometer was utilized to monitor the photocatalytic behaviour of MnT nanocomposites. The photocatalytic tests were carried out with an aqueous solution of malachite green oxalate (molecular formula $C_{52}H_{54}N_4O_{12}$, PubChem, CAS 2437-29-8) as the test contaminant in a reaction chamber enclosed within a wooden chamber fitted with UV lamps (Philips TUV 30 W T8). Arrangement of the reactor was such that UV light was directly incident on the samples. The photon flux has been calculated by a method discussed in M.D. Purkayastha et al. [2]. Prior to photocatalytic experiments, the aqueous dye solution was subjected to UV irradiation for 1 h to check whether photolysis occurs. Also, the adsorption behaviour of the photocatalysts for MG dye was tested without UV light irradiation. To achieve this, the photocatalysts were dispersed in the aqueous dye solution and stirred in dark for 1 h. The photocatalytic activities of both the samples were evaluated by measuring the decomposition of MG under UV light with time. Typically, 50 mL aqueous solution of MG dye (0.001 M) with 50 mg of the photocatalyst was stirred in the reactor. Prior to stirring, the system was dispersed by ultrasonic waves. After subjecting to UV irradiation, 5 mL aliquots of the reaction solutions were removed from the reactor every 10 min for analysis. These aliquots were centrifuged at 1000 rpm to exclude suspended particles, and the concentration of MG in the supernatant solutions was assessed by UV–Vis spectrometry at 618 nm, 315 nm and 418 nm absorption wavelengths for MG.

To analyse the influence of ultrasound on the behaviour of oxidizing species, photocatalytic degradation kinetic tests were repeated with optimal amounts of hydrogen peroxide (2 mL) added to S-MnT catalyst once directly and once after ultrasonication.

3 Results and discussion

3.1 S-MnT synthesis

Sonochemical methods of synthesis have been recently considered as a simple and efficient with the non-requirement of surfactants and complexing agents [25]. Addition of NaOH causes hydrolysis of titanium tetrabutoxide [Eq. (1)]. The hydrolytic species undergoes condensation and aggregation forming TiO_2 under the effect of sonication at an elevated temperature of 80 °C [13, 26, 27].



Regarding the formation of Mn_2O_3 , the precursor manganese acetate tetrahydrate is first dissolved in ethanol where it undergoes hydrolysis [9]. The use of stearic acid can modify the particle surface by introducing characteristic groups onto the surface of Mn_2O_3 to alter its physicochemical properties [28]. Also, the long carbon chains in stearic acid endow it with strong ability to disperse metal precursors [29]. The FTIR spectrum confirms the modification by showing a band corresponding to stearate. Similar predictions have been made by Kolodziejczak-Radzimska et al. [30]. Probably, changes in pressure and temperature due to ultrasonic irradiation caused Mn^{2+} ions to get oxidized to Mn_2O_3 that impeded the TiO_2 particles to join forming rod like structures [31]. Similar observations have been made by Hu et al. [25] who synthesized connected rods of ZnO using a sonochemical process with an aqueous solution of $Zn(NO_3)_2 \cdot 6H_2O$ at a temperature of 80 °C under ambient conditions.

3.2 Structural characterization

The diffraction pattern (Fig. 1a) of the pure TiO_2 shows the presence of anatase peaks corresponding to the (1 0 1), (0 0 4), (2 0 0), (1 0 5), (2 1 1), (2 0 4), (1 1 6), (2 2 0) and (2 1 5) diffraction planes supported by JCPDS card no.78-2486. Figure 1b, c depicts the XRD patterns acquired from the two representative samples H-MnT and S-MnT. The diffraction peaks can be indexed to the mixtures of TiO_2 anatase and bixbyite structure of Mn_2O_3 coinciding with JCPDS 24-0508. The S-MnT and H-MnT nano powders exhibited brown hue.

Sonication effect on size of the crystallites, and the phase was studied from the XRD pattern [32]. Both the

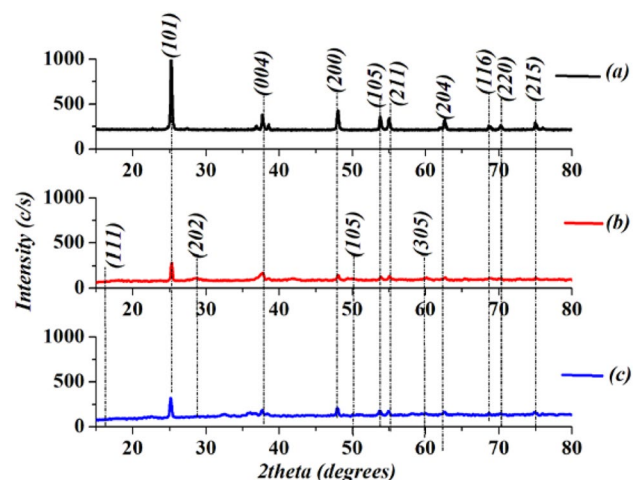


Fig. 1 XRD patterns of **a** TiO_2 , **b** H-MnT and **c** S-MnT

composites favoured anatase phase of TiO_2 in it. As shown in Fig. 1, the intensity of the (101) peak of TiO_2 in the composites decreased remarkably in comparison to pure TiO_2 anatase. However, the peaks of H-MnT appeared slightly sharper in comparison to S-MnT showing signs of improved crystalline structure. Probably, the step-wise hydrolysis of tetrabutyl titanate affected the process of crystallization in S-MnT. It could be concluded from this that ultrasound had some impact on the crystallinity. On calculating the crystallite size by Scherer formula [33] corresponding to the most intense (101) peak of TiO_2 in the composites, it was observed that sizes (31.94 nm for H-MnT and 24.18 nm for S-MnT) are comparable. Overall,

sonosynthesis has little or no influence on crystallite size and phase of the synthesized samples.

The energy dispersive X-ray (EDS) spectra of both H-MnT (Fig. 2a) and S-MnT (Fig. 2b) confirm the presence of manganese (5.6–6.6 keV), titanium (4.5–5 keV) and oxygen (0–1 keV) [34]. It can be observed that the atomic weight percentage of manganese in S-MnT is much higher which suggests better dispersion of manganese in the formation of S-MnT composite.

The typical FESEM images of the as-synthesized samples presented in Fig. 2 shows that the morphology changes drastically with change in synthesis techniques. The sample S-MnT prepared with ultrasound generated

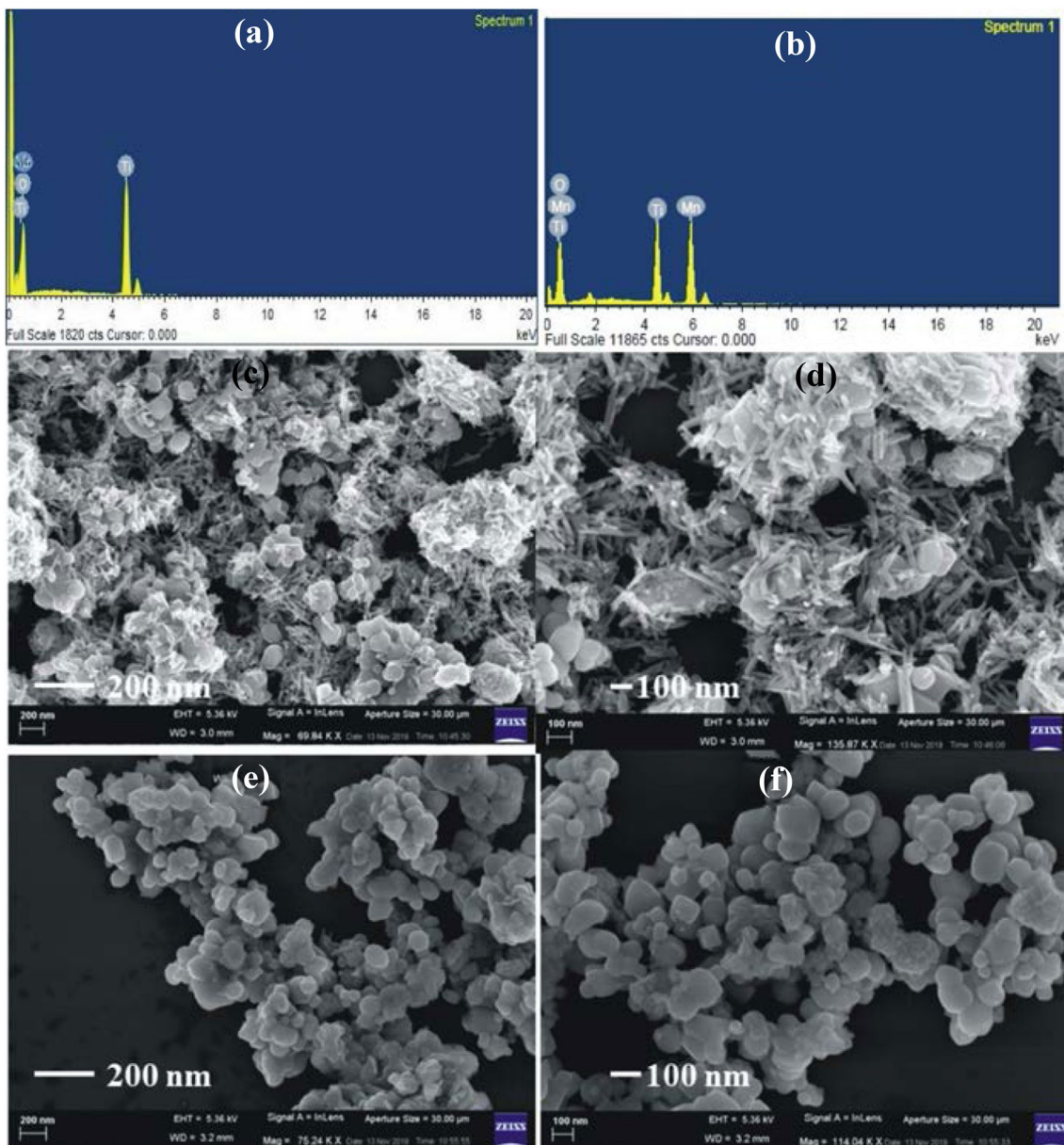


Fig. 2 **a** EDS image of H-MnT; **b** EDS image of S-MnT; **c** and **d** FESEM images of S-MnT and **e** and **f** FESEM images of H-MnT

nanorods along with nanodisks (Fig. 2c, d), while only hexagonal nanodisks could be observed for H-MnT (Fig. 2e, f). It should be noted that these composite structures were synthesized maintaining all experimental conditions fixed except the use of ultrasound. Therefore, the evolution of diverse morphology is believed to be the result of ultrasound. The existence of diverse morphology in S-MnT could be because manganese impeded the hexagonal nanodisks to grow along preferred crystallographic direction forming nanorods under the influence of ultrasound. Thus, sonosynthesis can significantly influence the surface morphology of the nanoparticles which may have a profound effect on photocatalytic activity as well [35, 36].

The samples were dispersed in doubly distilled water in an ultrasonic bath and the absorbance spectrum was recorded (Fig. 3i). H-MnT showed absorption peaks at 238 nm and 377 nm corresponding to the UV region. These are characteristics peaks of TiO₂ and found to coincide well with literature [37, 38]. Similar peaks were observed in the case of S-MnT. But the peak at 377 nm appeared red shifted by 5 nm. The Tauc Eq. (3) was utilized to calculate the optical band gap (E_g).

$$\alpha h\nu = C(h\nu - E_g)^n \quad (3)$$

where α is the absorption coefficient and n signals the character of transition which assumes a value 1/2 for direct, allowed transition. The band gap of H-MnT was found to 2.44 eV (Fig. 3ii). The synergistic effect of ultrasound brings down the band gap energy to 2.14 eV for S-MnT (Fig. 3iii). Probably, ultrasound caused chemical bonding between Mn₂O₃ and TiO₂ particles in the composite that led to band gap narrowing. The band gap energy values are lower than those reported by other researchers [39] which could be due to structural distortion resulting from oxygen deficiencies in the samples. Also, the S-MnT peaks showed higher intensity confirming the structural modification. Thus, sonochemistry is capable of tuning the

band gaps and altering the light absorption properties of the samples as well.

IR spectra of S-MnT and H-MnT are illustrated in Fig. 4i. The peaks at 3400 cm⁻¹ and 1627 cm⁻¹ in both the samples can be assigned to the stretching vibrations of adsorbed water molecules and OH⁻ in the lattice. H-MnT and S-MnT both show the characteristic peak of stearic acid at 1046 cm⁻¹ used in their preparation which confirms that stearic acid is well incorporated in the structures [40]. The formation of bonds between metal and oxygen are confirmed from the peaks at 514 cm⁻¹ and 730 cm⁻¹ [29, 40].

Manganese, being a transition metal ion, has a wide emission wavelength range and its location in the TiO₂ lattice actually decides its luminescence properties [41]. The photoluminescence (PL) properties of the samples under the UV excitation wavelength of 300 nm are presented in Fig. 4ii. Considering the Tanabe-Sugano diagrams [42] to demonstrate the PL mechanism, it can be assumed that due to UV excitation, electron transition occurs and the system is excited from the ⁴A₂ ground state to the excited states of ²T₁ and ⁴T₂. These excited states are however not stable, and it is presumable that the system will relax and ultimately come down to the ground state ⁴A₂ through a radiative transition. Previous studies have reported that a material can emit light corresponding to different wavelengths based on their arrangement within the lattice [43, 44]. H-MnT showed emissions at 469 nm and 551 nm while for S-MnT (Fig. 4ii) these peaks appeared slightly red shifted. This red shift can be attributed to the evolution of defects [45]. The peak at 551 nm corresponds to yellow-orange (and also red) emission and is associated with deeper defects while that at 469 nm corresponds to blue-green emission which can be associated with surface defects [46, 47]. Manganese is known to have variable oxidation states. Report [48] claims that the emission band of Mn⁴⁺ ion stretches from 600 to 710 nm and is due to the ²E → ⁴A₂ transition. In the present case, a peak at 692 nm confirms the presence of Mn⁴⁺ ions in both

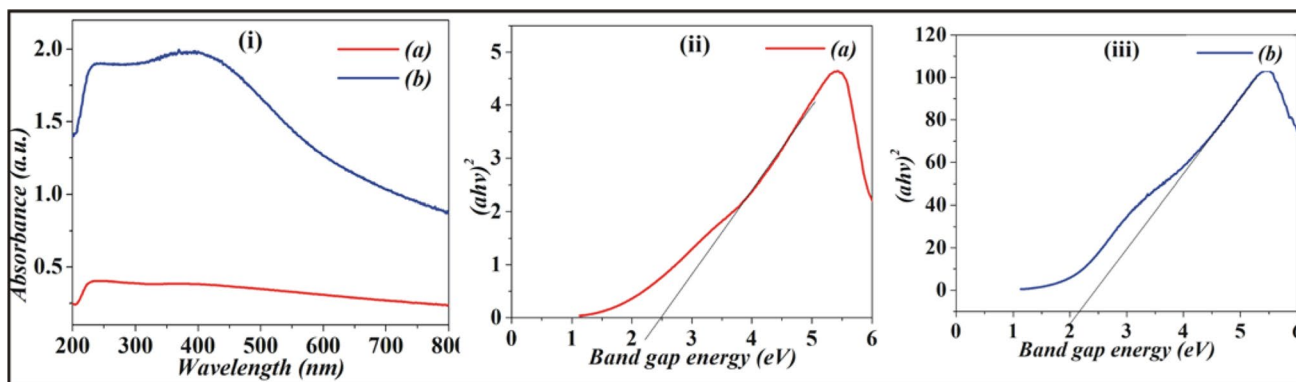


Fig. 3 (i) Absorption spectra of (a) H-MnT and (b) S-MnT; (ii) & (iii) Band gap determination using Tauc plot of (a) H-MnT and (b) S-MnT

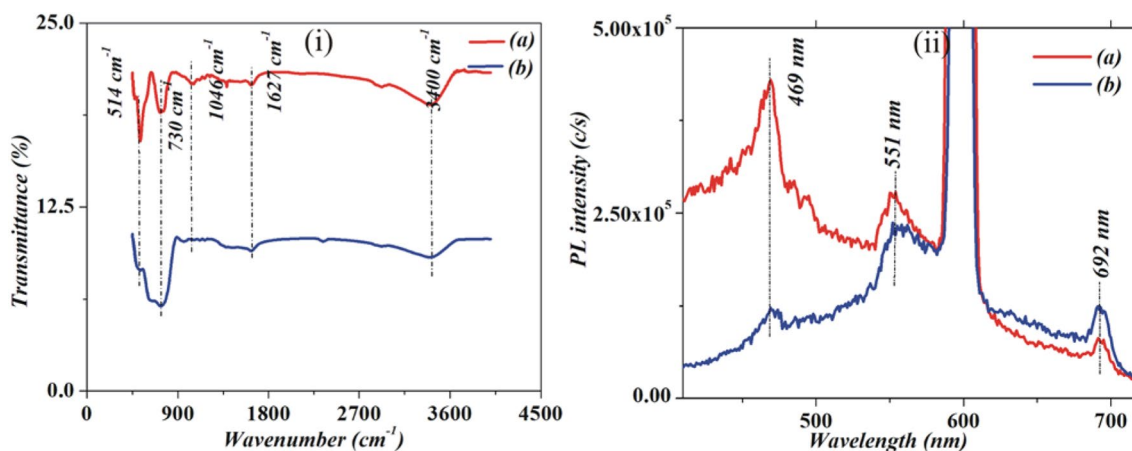


Fig. 4 (i) Infrared spectra of (a) H-MnT and (b) S-MnT; (ii) Emission spectra of (a) H-MnT and (b) S-MnT

the composites. Generally, the octahedral coordinated Mn²⁺ ions are known to yield an orange to red emission, whereas tetrahedral coordinated ones exhibit a green emission [49–51]. Thus, PL spectra confirm the presence of both octahedral coordinated Mn²⁺ ions and tetrahedral coordinated Mn²⁺ ions in the composites.

3.3 BET analysis results

The synthesized S-MnT sample (Fig. 5a) indicated type IV isotherm according to IUPAC classification and exhibited H-2 type hysteresis loop corresponding to mesoporous nature [52]. It also indicates the existence of narrow slit shaped pores [52]. At a relative pressure of 0.05, the first layer on the sample surface gets filled up which is indicated by the first inflection point A. The linear region (B) in the isotherm is attributed to the multilayer adsorption on the surface. BET method has been utilized to estimate the surface area using multi-point BET Eq. (4) indicated as follows: [52]

$$\frac{1}{W \left[\frac{P_0}{P} - 1 \right]} = \frac{1}{W_m C} + \frac{C - 1}{W_m C} \left(\frac{P}{P_0} \right), \tag{4}$$

where W_m indicates the adsorbate weight covering the surface and W is the gas accumulated at P/P₀. By plotting 1/[W (P/P₀) – 1] versus P/P₀, we obtained a linear curve (Fig. 5b) within 0.05 < P/P₀ < 0.35 range. This proves that the isotherm data conforms well to the BET model.

The BJH method was then employed to determine the pore size distribution (Fig. 5c).

The surface area value for S-MnT is 18.14 m²/g. It is well known that mesopores and high surface area are beneficial for the adsorption and diffusion of the reactants [9]. As surface area increases, light harvesting capacity of the photocatalyst increases [53] which cause a significant increase in the interfacial charge transfer rate [54]. Also, the availability of active surface area differs depending on nanostructure dimensions [55]. Peter et al. [56] observed that reduction in dimensionality enhanced the available active surface area. S-MnT also shows a wider PSD which

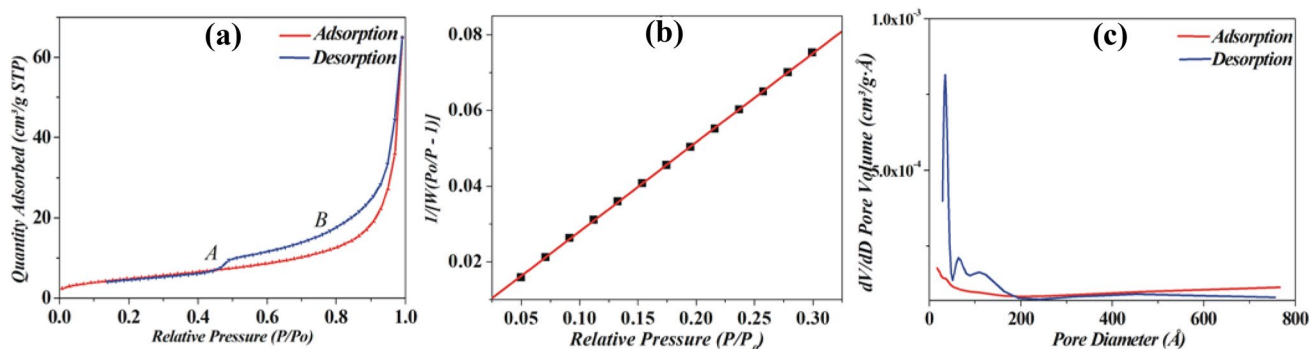


Fig. 5 a Adsorption–desorption isotherm of S-MnT b BET surface area linear plot of S-MnT c Differential mesopore pore size distribution (BJH method) of S-MnT

is suitable for energy applications and environmental remediation.

3.4 Analysis of photocatalytic properties

Malachite green (MG) is an organic pollutant present in aquatic ecosystems widely used in agriculture as a biocide [57]. The photocatalytic behaviour of the composites was analysed by monitoring their MG decomposition rates under UV radiation at neutral pH. The UV irradiation dose has been calculated as discussed in [2] and listed in Table 1. Dark experiments were carried out for 1 h and the adsorption ability of the composites was found to be less than 10% (Fig. 6i). Negative control experiments (without catalyst) were carried out and decomposition was found to be negligible in absence of photocatalyst. The MG solution along with the added photocatalyst was then subjected to UV irradiation and the progress of the reaction was followed by monitoring the intensity of MG absorption bands at 618 nm, 315 nm and 418 nm respectively. A change in absorbance intensity as function of time was observed (Figure S1). The kinetics of

heterogeneous catalytic processes can be best described by Langmuir–Hinshelwood model that takes the sorption effect into consideration. Dye molecules tend to get adsorbed on the active sites of the photocatalyst before the reaction starts [58]. The expression for rate of the reaction (5) that changes with time is given by [59]

$$r = -\frac{dA}{dt} = \frac{k_r KA}{1 + KA} \tag{5}$$

where A is the dye concentration at any time t, A₀ is the initial dye concentration, k_r is the reaction rate constant and K is the adsorption coefficient of the dye MG. Rate of photodegradation of organic compounds, in general, follow first order reaction kinetics. For pseudo first order reaction (KA ≪ 1)

$$\frac{dA}{dt} = -k_r KA \tag{6}$$

$$\frac{dA}{dt} = -k_1 A \tag{7}$$

where k₁ is the pseudo first order reaction rate constant. To make the concentration–time relationship linear

Table 1 Calculated parameters of photocatalytic activity for MnT nanocomposites

Sample type	Time (min)	UV radiation dose (10 ⁻⁸) (Jsm ²)	Degradation efficiency PD (%)	Pseudo first order rate constant (k ₁) min ⁻¹		Correlation coefficient R ²	Error χ ²
				1st cycle (As such)	5th cycle (Recycled)		
H-MnT	60	3.451	92.14	.0445	.0399	.9747	5.655
S-MnT	60	3.451	99.61	.0788	.0689	.9576	18.08
S-MnT with sonicated H ₂ O ₂	50	2.397	99.61	.0815	.0883	.9861	15.33
S-MnT with directly added H ₂ O ₂	30	2.397	91.31	.0986	.0795	.9670	2.130

Up to four significant figures except time

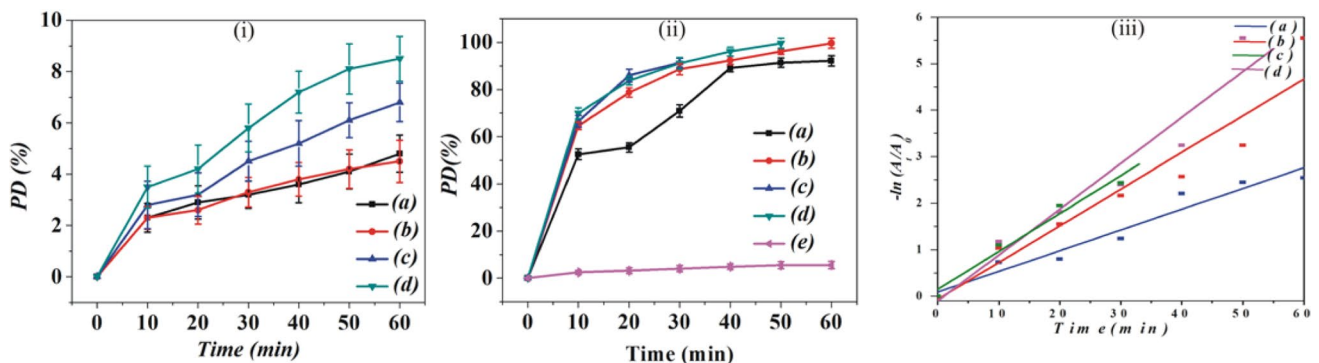


Fig. 6 (i) Dark experiments to investigate adsorption behaviour (ii) Photocatalytic MG contaminant decomposition efficiency and (iii) Reaction rate evaluation plot of (a) H-MnT and (b) S-MnT (c) S-MnT

with directly added H₂O₂ (d) S-MnT with sonicated H₂O₂ and (e) no photocatalyst

$$\ln \left(\frac{A_t}{A_0} \right) = -k_1 t. \tag{8}$$

On plotting $-\ln(A_t/A_0)$ as a function of time, the constant k_1 can be easily determined from the slope of linear best fit. The decolourization efficiency was calculated using [60]

$$PD = \frac{(A_0 - A_t)}{A_0} \times 100, \tag{9}$$

where A_0 and A_t denote dye concentrations before and after photo-irradiation. Figure 6ii shows the time dependent percentage decolourization efficiency (PD) of MG solution (100 mg/L) under UV irradiation in contact with the composites, and also without the presence of the photocatalyst for MG 618 nm absorption peak. The PD values corresponding to 315 nm and 418 nm peaks of MG have been provided in Table S1 in Supplementary material. The composites were found to exhibit enhanced photoactivity in comparison to similar reported materials under UV radiation [61, 62]. It has already been discussed that H_2O_2 is a promising electron acceptor that tends to enhance the overall reaction rate [63]. However, addition of H_2O_2 in large amounts can have a deteriorating effect on it [64, 65]. Experiments were carried out with different amounts of H_2O_2 (0.5-5 mL) and 2 mL H_2O_2 was found to be the optimal dosage. To underline the sonication effect, this H_2O_2 was added in two ways—once directly and once after being sonicated. S-MnT with sonicated H_2O_2 showed the best photoactivity which confirmed that sonochemistry has a role in inhibition of electron–hole recombination. Probably, sonochemistry led to the uniform dispersion of H_2O_2 in the photocatalyst solution which accelerated the process of radical formation. The estimated values of k_1 , corresponding correlation coefficients (R^2), PD efficiencies and error (chi-square χ^2) values are listed in Table 1 (for pseudo first order). Figure 6iii provides the values of the pseudo first order rate constant obtained from the linear regression curves.

The stability is essential for its practical application. A cycle experiment of degrading MG in aqueous solutions over the composites was conducted. Results (Table 1) showed that S-MnT with sonicated H_2O_2 still held high photocatalytic activity after five cycles (Fig. 7).

The mechanism of photocatalysis is described as follows: On irradiating the reaction solution with UV light, photoexcited charge carriers get formed (Eq. (10)).

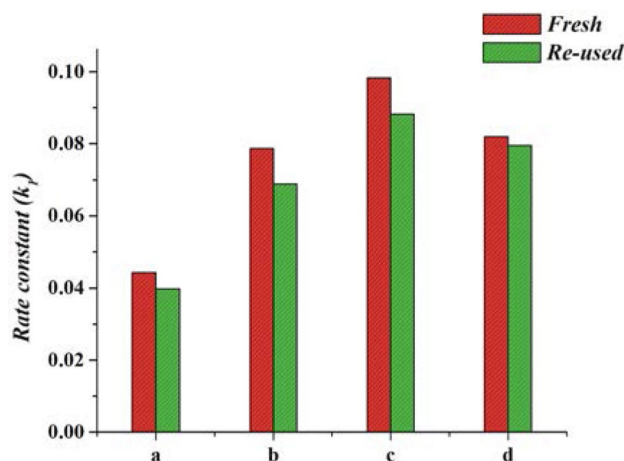
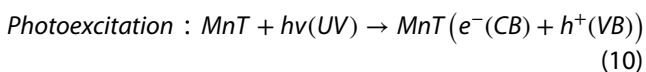
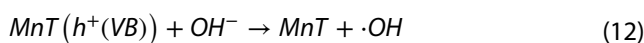


Fig. 7 Rate constant comparison plot for of a H-MnT and b S-MnT c S-MnT with sonicated H_2O_2 and d S-MnT with directly added H_2O_2

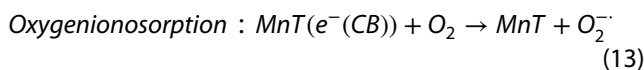
where $h\nu$ = photons, h^+ = holes, proton = H^+ , CB is conduction band, VB is valence band and e^- = electrons.

Magesh et al. [66] calculated the conduction band potential (E_{CB}) for TiO_2 ($E_g = 3.2$ eV) in reference to normal hydrogen electrode (NHE) as -0.29 eV while Li et al. [67] found that E_{CB} for Mn_2O_3 ($E_g = 3.2$ eV) is -1 eV. Clearly, E_{CB} for Mn_2O_3 is more negative than that of TiO_2 . So, it is expected that at the junction of the MnT composite, there will be a transfer of excited electrons from Mn_2O_3 to the conduction band of TiO_2 .

The holes in the valence band will give rise to $\cdot OH$ radicals by the oxidation of water as given by Eqs. (11) and (12).



Some excited electrons may get transferred to adsorbed oxygen molecules reducing molecular oxygen to superoxide radicals (O_2^-) [23, 68–71].



Also, as E_{CB} for TiO_2 is more negative than that for O_2/H_2O_2 (0.682 eV vs NHE), H_2O_2 may be produced in the process [72].



In case of added H_2O_2 , Ti-peroxo species tend to be formed at the solution interface [73–76]. Ohno et al. [75] through FTIR and X-ray photoelectron spectroscopy (XPS) and Lousada et al. [77] through density functional theory studies have confirmed the formation of such peroxo

Table 2 Comparison of photocatalytic abilities of some composites for MG degradation

Photocatalyst	Dye conc (mg/L)	Catalyst dose (g/L)	PD (%)	Time (min)	Light source	References
TiO ₂ rutile	100.0	0.050	97.00	180	UV	[2]
Commercial TiO ₂	100.0	0.050	96.00	210	UV	[2]
TiO ₂ -DAS	–	0.005	60.40	120	UV	[3]
TiO ₂ -DAS-SiO ₂	–	0.005	21.60	120	UV	[3]
MnS	–	0.005	–	80	UV	[81]
MnS	–	0.050	56.60	300	UV	[82]
MnS-DAS	–	0.050	82.80	300	UV	[82]
–	12.50	–	70.00	120	Ultrasound (135 W)	[83]
TiO ₂	10.00	0.100–0.500	100.0	30–60	UV + Ultrasound	[83]
A. Flavus	0.030	–	99.70	8640	–	[84]
A. Solani	0.030	–	91.70	8640	–	[84]
ZnS:Mn	2.000	–	91.00	60	Visible	[85]
ZnS:Mn/ZnS	2.000	–	98	60	Visible	[85]
Au/NaNbO ₃	100.0	0.8–1.6	87.00–94.00	60	Visible	[86]
Ca doped ceria	6.000	0.100	93.00	90	UV	[87]
ZnO capped with ethylene diamine tetra acetic acid	9.270	0.002	94.10	41	Simulated sunlight	[88]
ZnO capped with citric acid	9.270	0.002	80.10	61	Simulated sunlight	[88]
ZnO capped with oleic acid	9.270	0.002	67.60	61	Simulated sunlight	[88]
Nickel vanadate	927.0	0.100	–	100	Visible	[89]
TiO ₂	50.00	0.500	99.90	240	UV	[90]
CoTiO ₃	–	–	96.30	180	UV	[3]
Co ₂ TiO ₄	–	–	88.00	200	UV	[3]
ZnO nanorods on RGO/Ni foam	20.00	–	100.0	15	UV	[91]
ZnO/Ni foam	20.00	–	68.00	15	UV	[91]
RGO/Ni foam	20.00	–	38.00	15	UV	[91]
H-MnT	927.0	0.050	92.10	60	UV	Present work
S-MnT	927.0	0.050	99.60	60	UV	Present work
S-MnT with direct H ₂ O ₂	927.0	0.050	91.30	30	UV	Present work
S-MnT with sonicated H ₂ O ₂	927.0	0.050	99.60	50	UV	Present work

Up to 4 significant figures except time

species. These reactive oxygen species (OH, O₂⁻; H₂O₂ and peroxy species) ultimately lead to transformation of the chromophoric groups in the dye. MG is a dye containing nitrogen. Depending on the oxidation state of the nitrogen atom, MG may release NH₄⁺, NO₃⁻ or even N₂ [78]. However, the complete mineralization of the dye requires highly energetic free radicals which are preferentially generated under UV irradiation. In this context, Bae et al. [79] has documented that the TOC removal efficiencies of titanium based catalysts are much higher under UV irradiation.

Also, the defect content in the composites could be responsible for the efficient photoactivity shown by them. In this regard, Zheng et al. [80] have explained that defects like interstitial oxygen generate shallow levels near the valence band while defects like oxygen vacancies act as electron acceptors. Thus, interfacial charge transfer prolongs the lifetime of the carriers by suppressing the

recombination of electron–hole pairs. However, in the future, such parameters need to be studied on a theoretical platform.

A comparison of photocatalytic ability of synthesized MnT composites with other reported composites in degrading MG is illustrated in Table 2.

4 Conclusions

The present study outlined a reliable, cost-effective sonochemical method to synthesize binary nanocomposites of manganese and titanium oxides that can be extended for the preparation of other binary metal oxide composites. The composites were used to test the photocatalytic degradation of MG in the aqueous solution. The decolorization rate of S-MnT photocatalyst with ultrasound

functionalized H_2O_2 was found to be higher than that of H-MnT, bare S-MnT and S-MnT with directly added H_2O_2 . It could be proposed that unique nanorod–nanodisk morphology, defect concentration and sonochemistry played a vital role in reducing the chances of electron hole recombination thereby enhancing pollutant degradation rate. Luminescence studies also predict possible optoelectronic applications for transition metal oxide nanomaterials. The composites exhibited good stability predicting potential applications in waste water treatment, environment protection and even in energy preservation.

Acknowledgements Authors highly appreciate the DST-PURSE program of Kalyani University and the DST-FIST Project (SR/FST/PSI-175/2012). The authors are indebted to Dr Sayan Bhattacharyya, IISER Kolkata for surface area measurements. Sincere acknowledgement is due for the assistance under DST-FIST and UGC-SAP programs to the Dept. of Chemistry, Kalyani University. Gopala Krishna Darbha is thankful to the support from SERB, Ramanujan Fellowship Grant (SB/S2/RJN-006/2016) and SERB-ECR project (ECR/2017/000707), India.

Compliance with ethical standards

Conflict of interest The authors declare that they have no conflict of interest.

References

- Soler-Illia GJAA, Sanchez C, Lebeau B, Patarin J (2002) Chemical strategies to design textured materials: from microporous and mesoporous oxides to nanonetworks and hierarchical structures. *Chem Rev* 102:4093–4138
- Purkayastha MD, Mridha S, Datta J, Ray PP, Biswas BD, Sarkar M, Darbha GK, Singh N, Majumder TP, Saha P, Das D (2019) The carrier transport properties and photodegradation ability of low temperature synthesized phase pure rutile titanium oxide nanostructured materials. *Chem Phys* 226:362–370
- Purkayastha MD, Sarkar M, Majumder TP (2019) Enhanced UV shielding properties of DAS based nanocomposites. *Optik (Stuttg)* 182:469–478
- Purkayastha MD, Ray PP, Majumder TP, Sarkar M (2019) Spectroscopic characterization and photocatalytic degradation ability of ternary oxides of cobalt. *Int J Innov Res Phys* Accept Artic
- Purkayastha MD, Singh N, Darbha GK, Majumder TP (2020) Strain influence on the structural properties of nitrogen and fluorine codoped TiO_2 . *Optik (Stuttg)* 206:164029
- Harir M, Gaspar A, Kanawati B, Fekete A, Frommberger M, Martens D, Kettrup A, El Azzouzi M, Schmitt Kopplin P (2008) Photocatalytic reactions of imazamox at TiO_2 , H_2O_2 and $\text{TiO}_2/\text{H}_2\text{O}_2$ in water interfaces: kinetic and photoproducts study. *Appl Catal B Environ* 84:524–532
- Sivakumar S, Selvaraj A, Ramasam AK, Balasubramanian V (2013) Enhanced photocatalytic degradation of reactive dyes over $\text{FeTiO}_3/\text{TiO}_2$ heterojunction in the presence of H_2O_2 . *Water Air Soil Pollut* 224:1529–1542
- Song ZQ, Wang SB, Yang W, Mo L, Wang H, Yan H (2004) Synthesis of manganese titanate MnTiO_3 powders by a sol-gel hydrothermal method. *Mater Sci Eng, B* 113:121–124
- Xue M, Huang L, Wang JQ, Wang Y, Gao L, Zhu JH, Zou ZG (2008) The direct synthesis of mesoporous structured $\text{MnO}_2/\text{TiO}_2$ nanocomposite: a novel visible light active photocatalyst with large pore size. *Nanotechnology* 19:185604
- Li J, Zeng HC (2006) Preparation of monodisperse Au/TiO_2 nanocatalysts via self-assembly. *Chem Mater* 18:4270–4277
- Kharkwal M, Uma S, Nagarajan R (2010) Use of a chelating agent for the synthesis of high surface area pyrophanite MnTiO_3 powders. *Mater. Lett.* 64:692–694
- Sinha AK, Suzuki K (2005) Preparation and characterization of novel mesoporous ceria-titania. *J Phys Chem B* 109:1708–1714
- Ghows N, Entezari MH (2010) Ultrasound with low intensity assisted the synthesis of nanocrystalline TiO_2 without calcination. *Ultrason Sonochem* 17:878–883
- Guo J, Zhu S, Chen Z, Li Y, Yu Z, Liu Q, Li J, Feng C, Zhang D (2011) Sonochemical synthesis of TiO_2 nanoparticles on graphene for use as photocatalyst. *Ultrason. Sonochem* 18:1082–1090
- Arenas MC, Rodriguez-Nunez LF, Rangel D, Martinez-Alvarez O, Martinez-Alonso C, Castano VM (2013) Simple one step ultrasonic synthesis of anatase titania/polypyrrole nanocomposites. *Ultrason. Sonochem* 20:777–784
- Vinoth R, Karthik P, Devan K, Neppolian B, Muthupandian AK (2017) TiO_2 - NiO p–n junction nanocomposite with enhanced sonophotocatalytic activity under diffused sunlight. *Ultrason. Sonochem* 35:655–663
- Tryba B, Toyoda M, Morawski AW, Nonaka R, Inagaki M (2007) Photocatalytic activity and 'OH radical formation on TiO_2 in the relation to crystallinity. *Appl Catal B* 71:163–168
- Tachikawa T, Majima T (2010) Single molecule, single particle fluorescence imaging of TiO_2 based photocatalytic reactions. *Chem Soc Rev* 39:4802–4819
- Fujihira M, Satoh Y, Osa T (1981) Heterogeneous photocatalytic oxidation of aromatic compounds on titanium dioxide. *Nature* 298:206–208
- Kim W, Tachikawa T, Moon G, Majima T, Choi W (2014) Molecular-level understanding of the photocatalytic activity difference between anatase and rutile nanoparticles. *Angew Chem Int Ed* 53:14036–14041
- Hirakawa T, Yawata K, Nosaka Y (2007) Photocatalytic reactivity for O_2^- and 'OH radical formation in anatase and rutile TiO_2 suspension as the effect of H_2O_2 addition. *Appl Catal A* 325:105–111
- Zhang J, Nosaka Y (2014) Mechanism of the OH radical generation in photocatalysis with TiO_2 of different crystalline types. *J Phys Chem C* 118:10824–10832
- Kakuma Y, Nosaka A, Nosaka Y (2015) Difference in TiO_2 photocatalytic mechanism between rutile and anatase studied by the detection of active oxygen and surface species in water. *Phys Chem Chem Phys* 17:18691–18698
- Nosaka Y, Nosaka A (2016) Chapter 7: Kinetic processes in the presence of photogenerated charge carriers. In: Schneider J, Bahnemann D et al (eds) *Photocatalysis: fundamentals and perspectives*. Royal Society of Chemistry, London, pp 165–184
- Hu XL, Zhu YJ, Wang SW (2004) Sonochemical and microwave assisted synthesis of linked single crystalline ZnO rods. *Mater Chem Phys* 88:421–426
- Prasad K, Pinjari DV, Pandit AB, Mhaske ST (2010) Phase transformation of nanostructured titanium dioxide from anatase to rutile via combined ultrasound assisted sol-gel method. *Ultrason Sonochem* 17:409–415
- Ling J, Wang K, Wang Z, Huang H, Zhang G (2019) Enhanced piezoelectric-induced catalysis of SrTiO_3 nanocrystal with well-defined facets under ultrasonic vibration. *Ultrason Sonochem.* <https://doi.org/10.1016/j.ultsonch.2019.104819>
- Kockmann A, Hesselbach J, Zellmer S, Kwade A, Garnweitner G (2015) Facile surface tailoring of metal oxide nanoparticles via a two-step modification approach. *RSC Adv* 5:60993–60999

29. Enhessari M, Parviz A, Karamali E, Ozaee K (2012) Synthesis, characterisation and optical properties of MnTiO₃ nanopowders. *J Exp Nanosci* 7:327–335
30. Kolodziejczak-Radzimska A, Jesionowski J (2014) Zinc oxide—from synthesis to application: a review. *Materials (Basel)* 7:2833–2881
31. Elser MJ, Berger T, Brandhuner D, Bernardi J, Diwald Knozinger E (2006) Particles coming together: electron centres in adjoined TiO₂ nanocrystals. *J Phys Chem* 110:7605–7608
32. Monatzer M, Behzadnia A, Pakdel E, Rahimi MK, Moghadam MB (2011) Photoinduced silver on nano titanium dioxide as an enhanced antimicrobial agent for wool. *J Photochem Photobiol, B* 103:207–214
33. Patterson AL (1939) The Scherrer formula for x-ray particle size determination. *Phys Rev* 56:978–982
34. Das SK, Rou BK (2015) Magnetic and ferroelectric properties of Zn and Mn co-doped BaTiO₃. *Chin Phys B* 24:067702
35. Smith AM, Nie S (2010) Semiconductor nanocrystals: structure, properties, and band gap engineering. *Acc Chem Res* 43:190–200
36. Zhang H, Zhu H, Sun R (2012) Fabrication of photocatalytic TiO₂ nanoparticle film on PET fabric by hydrothermal method. *Text Res J* 82:747–754
37. Linsebigler AL, Lu G, Yates JT (1995) Photocatalysis on TiO₂ surfaces: principles, mechanisms and selected results. *Chem Rev* 95:735–758
38. Binas V, Venieri D, Kotzias D, Kiriakidis G (2017) Modified TiO₂ based photocatalysts for improved air and health quality. *J Materomics* 3:3–16
39. Sharrouf M, Awad R, Roumie M, Marhaba S (2015) Structural, optical and room temperature magnetic study of Mn₂O₃ nanoparticles. *Mater Sci Appl* 6:850–859
40. Sharma YK, Kharkwal MK, Uma S, Nagarajan R (2009) Synthesis and characterisation of titanates of the formula MnTiO₃ (M = Mn, Fe Co, Ni, Cd) by co-precipitation of mixed metal oxalates. *Polyhedron* 28:579–585
41. Gupta SK, Kadam RM, Gupta R, Sahu M, Natarajan V (2014) Evidence for stabilisation of manganese ion as Mn(II) and Mn(IV) in α -Zn₂P₂O₇: Probed by EPR, luminescence and electrochemical studies. *Mater Chem Phys* 145:162–167
42. Tanabe Y, Sugano S (1954) On the absorption spectra of complex ions. *J Phys Soc* 9:753–766
43. Ye T, Dong Z, Zhao Y, Yu J, Wang F, Guo S, Zuo Y (2011) Controllable fabrication of perovskite SrZrO₃ hollow cuboidal nanoshells. *Cryst. Eng Commun* 13:3842–3847
44. Pathak N, Gupta SK, Ghosh PS, Arya A, Natarajan V, Kadam RM (2015) Probing local site environments and distribution of manganese in SrZrO₃: PL and EPR spectroscopy complimented by DFT calculations. *RSC Adv* 5:17501–17513
45. Raul SZ, Marcelino BF, Umapada P (2011) Photoluminescence and Raman scattering in Ag-doped ZnO nanoparticles. *J Appl Phys* 109:014308
46. Souza AE, Santos GTA, Barra BC, Macedo WD Jr, Teixeira SR, Santos CM, Senos AMOR, Amaral L, Longo E (2012) Photoluminescence of SrTiO₃: influence of particle size and morphology. *Cryst Growth Des* 12:5671–5679
47. da Silva LF, Avansi W, Moreira ML, Mesquita A, Maia LJQ, Andrés J, Longo E, Mastelaro VR (2012) Relationship between crystal shape, photoluminescence and local structure in SrTiO₃ synthesized by microwave assisted hydrothermal method. *J Nanomater* 2012:890397
48. Wang B, Lin H, Xu J, Chen H, Wang YS (2014) CaMg₂Al₁₆O₂₇: Mn⁴⁺ based red phosphor: a potential color converter for high-powered warm w-led. *ACS Appl Mater Interfaces* 6:22905–22913
49. Shang M, Geng D, Zhang Y, Li G, Yang D, Kang X, Lin J (2012) Luminescence and energy transfer properties of Ca₈Gd₂(PO₄)₆O₂: A (A = Ce³⁺/Eu²⁺/Tb³⁺/Dy³⁺/Mn²⁺) phosphors. *J Mater Chem* 22:19094–19104
50. Geng D, Li G, Sheng M, Yang D, Zhang Y, Cheng Z, Lin J (2012) Colour tuning via energy transfer in Sr₃In(PO₄)₃: Ce³⁺/Tb³⁺/Mn²⁺. *J Mater Chem* 22:14262–14271
51. Liu YF, Zhang X, Hao ZD, Wang XJ, Zhang JH (2011) Tunable full colour emitting Ca₃Sc₂Si₃O₁₂:Ce³⁺, Mn²⁺ phosphor via charge compensation and energy transfer. *Chem Commun* 47:10677–10679
52. Do DD (1998) Adsorption analysis: equilibrium and kinetics. Imperial College Press, London
53. Ahmed F et al (2014) Quantum-confinement induced enhancement in photocatalytic properties of iron oxide nanoparticles prepared by Ionic liquid. *Ceram Int* 40:15743–15751
54. Wei Z, Kowalska E, Verrett J, Colbeau-Justin C, Remita H, Ohtani B (2015) Morphology-dependent photocatalytic activity of octahedral anatase particles prepared by ultrasonication hydrothermal reaction of titanates. *Nanoscale* 7:12392–12404
55. Flores NM, Pal U, Galeazzi R, Sandoval A (2014) Effect of morphology, surface area and defect content on the photocatalytic dye degradation performance of ZnO nanostructures. *RSC Adv* 4:41099–41110
56. Peter JJ, Praveen E, Vignesh G, Nithiananthi P (2017) Zinc nanostructures with different morphology for enhanced photocatalytic activity. *Mater Res Express* 4:124003
57. Raval NP, Shah PU, Shah NK (2017) Malachite green 'a cationic dye' and its removal from aqueous solution by adsorption. *Appl Water Sci* 7:3407–3445
58. Delgado P, Sans MT, Beltvan S (2007) Kinetic study for esterification of lactic acid with ethanol and hydrolysis of ethyl acetate using an ion exchange resin. *Chem Eng J* 120:111–118
59. Herrmann JM (2010) Photocatalysis fundamentals revisited to avoid mis-conceptions. *Appl Catal B Environ* 99:461–468
60. Menzinger M, Wolfgang R (1969) The meaning and use of the Arrhenius activation energy. *Angew Chem* 6:438–444
61. Tateoka A, Sekine Y, Tsuda T, Ohashi T (2005) Manganese oxide photodeposited onto titanium dioxide as a new environmental catalyst. *Mater Sci Forum* 480/481 117:117–122
62. Subrahmanyam C, Magureanu M, Laub D, Renken A, Kiwi-Minsker L (2007) Nonthermal plasma abatement of trichloroethylene enhanced by photocatalysis. *J Phys Chem C* 111:4315–4318
63. Wong CC, Chu W (2003) The hydrogen peroxide assisted photocatalytic degradation of alachlor in TiO₂ suspensions. *Environ Sci Technol* 37:2310–2316
64. Ye H, Lu S (2013) Effect of hydrogen peroxide on the structure and photocatalytic activity of titania. *Res Chem Intermed* 41:139–149
65. Zang Y, Farnood R (2006) Effect of hydrogen peroxide on the photocatalytic degradation of tert-butyl ether. *Top Catal* 37:91–96
66. Magesh G, Viswanathan B, Viswanath RP, Varadarajan TK (2009) Photocatalytic behaviour of CeO₂–TiO₂ system for the degradation of methylene blue. *Indian J Chem* 48A:480–488
67. Li F, Wangyang P, Zada A, Humayun M, Wang B, Qu Y (2016) Synthesis of hierarchical Mn₂O₃ microspheres for photocatalytic hydrogen production. *Mater. Res Bull* 84:99–104
68. Sahel K, Elsellami L, Mirali I, Dappozze F, Bouhent M, Guillard C (2016) Hydrogen peroxide and photocatalysis. *Appl Catal B* 188:106–112
69. Jiang T, Wang K, Guo T, Wu X, Zhang G (2020) Fabrication of Z-scheme MoO₃/Bi₂O₄ heterojunction photocatalyst with enhanced photocatalytic performance under visible light irradiation. *Chin J Catal* 41:161–169
70. Sun X, Zhang J, Fu Z (2018) Polyoxometalate cluster sensitized with copper-viologen framework for efficient degradation of

- organic dye in ultraviolet, visible and near-infrared light. *ACS Appl Mater Interfaces* 10:35671–35675
71. Wang Z, Wang K, Li Y, Jiang L, Zhang G (2019) Novel BiSbO₄/BiOBr nanoarchitecture with enhanced visible light driven photocatalytic performance: oxygen-induced pathway of activation and mechanism unveiling. *Appl Surf Sci* 498:143850
 72. Mousavi M, Yangjeh AH, Abitorabi M (2016) Fabrication of novel magnetically separable nanocomposites using graphitic carbon nitride, silver phosphate and silver chloride and their applications in photocatalytic removal of different pollutants using visible light irradiation. *J Colloid Interface Sci* 480:218–231
 73. Regazzoni AE, Mandelbaum P, Matsuyoshi M, Schiller S, Bilmes SA, Blesa MA (1998) Adsorption and photooxidation of salicylic acid on titanium dioxide: a surface complexation description. *Langmuir* 14:868–874
 74. Li X, Chen C, Zhao J (2001) Mechanism of decomposition of H₂O₂ on TiO₂ surfaces using visible light irradiation. *Langmuir* 17:4118–4122
 75. Ohno T, Masaki Y, Hirayama S, Matsumura M (2001) TiO₂ photocatalyzed epoxidation of 1-decene by H₂O₂ under visible light. *J Catal* 204:163–168
 76. Pavel CC, Park S, Dreier A, Tesche B, Schmidt W (2006) Structural defects induced in ETS-10 by postsynthesis treatment with H₂O₂ solution. *Chem Mater* 18:3813–3820
 77. Lousada CM, Johansson AJ, Brinck T, Jonsson M (2012) Mechanism of H₂O₂ decomposition on transition metal oxide surfaces. *J Phys Chem C* 116:9533–9543
 78. Tanaka K, Padermpole K, Hisanaga T (2000) Photocatalytic degradation of commercial azo dyes. *Water Res* 34:327–333
 79. Bae S, Kim S, Lee S, Choi W (2014) Dye decolourization test for the activity assessment of visible light photocatalysts: realities and limitations. *Catal Today* 224:21–28
 80. Zheng YH, Chen CQ, Zhan YY, Lin XY, Zheng Q, Wei KM, Zhu JF, Zhu YJ (2007) Luminescence and photocatalytic activity of ZnO nanocrystals: correlation between structure and property. *Inorg Chem* 46:6675–6682
 81. Hussain W, Malik H, Hussain RA, Hussain H, Greens IR, Marwat S, Bahadur A, Iqbal S, Farooq MU, Li H, Badshah A (2019) Synthesis of MnS from single and multi-source precursors for photocatalytic and battery applications. *J Electron Mater* 48:2278–2288
 82. Biswas BD, Purkayastha MD, Majumder TP (2020) Effect of DAS on the optical and photocatalytic properties of metastable γ-MnS nanoparticles. *Surf Interfaces* 19:100469
 83. Berberidou C, Poullos I, Xekoukoulotakis NP, Mantzavinos D (2007) Sonolytic, photocatalytic and sonophotocatalytic degradation of malachite green in aqueous solutions. *Appl Catal B Environ* 74:63–72
 84. Ali H, Ahmad W, Haq T (2009) Decolourization and degradation of malachite green by *Aspergillus flavus* and *Alternaria solani*. *Afr J Biotechnol* 8:1574–1576
 85. Khaparde AR, Acharya AS (2018) Efficient photocatalytic degradation of malachite green dye under visible irradiation by water soluble ZnS:Mn/ZnS core/shell nanoparticles. *AIP Conf Proc* 1953:030139
 86. Baeissa ES (2016) Photocatalytic degradation of malachite green dye using Au/NaNbO₃ nanoparticles. *J Alloys Compd* 672:564–570
 87. Amar IA, Harara HM, Baqul QA, Qadir MAA, Altohami FA, Ahwidi MM, Abdalsamed IA, Saleh FA (2020) Photocatalytic degradation of malachite green dye under UV light irradiation using calcium-doped ceria nanoparticles. *Asian J Nanosci Mater* 3:1–14
 88. Meena S, Vaya D, Das BK (2016) Photocatalytic degradation of malachite green dye by modified ZnO nanomaterial. *Bull Mater Sci* 39:1735–1743
 89. Rathore R, Ameta R, Ameta SC (2014) Photocatalytic degradation of malachite green over nickel vanadate powder. *Acta Chim Pharm Indica* 4:213–220
 90. Chen CC, Lua CS, Chung YC, Jan JL (2007) UV light induced photodegradation of malachite green on TiO₂ nanoparticles. *J Hazard Mater* 141:520–528
 91. Wang Q, Zhang C, Zhou L, Zhang D, Tong Z, Liu Y, Chen J (2018) Efficient photocatalytic degradation of malachite green in sea water by the hybrid of ZnO nanorods grown on 3D reduced graphene oxide (RGO)/Ni foam. *Materials (Basel)* 11:1004

Publisher's Note Springer Nature remains neutral with regard to jurisdictional claims in published maps and institutional affiliations.